

DSD FRONT MODELS: NONIDEAL EXPLOSIVE DETONATION IN ANFO

John B. Bdzil, Tariq D. Aslam,
Richard A. Catanach and Larry G. Hill
Los Alamos National Laboratory
Los Alamos, New Mexico 87545

Mark Short
Department of Theoretical and Applied Mechanics
University of Illinois
Urbana, Illinois 61801

jbb@lanl.gov, aslam@lanl.gov,
richcat@lanl.gov, lgh@lanl.gov, short1@uiuc.edu

The DSD method for modeling propagating detonation is based on three elements: 1) a subscale theory of multi-dimensional detonation that treats the detonation as a front whose dynamics depends only on metrics of the front (such as curvature, etc.), 2) high-resolution, direct numerical simulation of detonation using Euler equation models, and 3) physical experiments to characterize multi-dimensional detonation propagation in real explosives and to provide data to calibrate DSD front models. In this paper, we describe our work on elements 1) and 3), develop a DSD calibration for the nonideal explosive ANFO and then demonstrate the utility of the ANFO calibration, with an example 3D detonation propagation calculation.

INTRODUCTION

The first Detonation Shock Dynamics (DSD) theory to be developed showed that the velocity of detonation normal to the shock, D_n , was solely a function of the shock curvature, κ . Referred to as the $D_n(\kappa)$ subscale detonation front law, this leading-order model pictured the flow as being a 1D, nozzle-like (spherically expanding), quasi-stationary flow. Non-uniformities in the flow experienced as one moved from place-to-place along the shock were neglected (no transverse flow variations) as were transient effects having to do with the inertia provided by the reaction-zone structure to instantaneous

acceleration of the detonation shock (no explicit time variations).

An analysis of the reaction zone flow, immediately adjacent to the inert material which provides confinement for the detonating explosive, showed that the angle between the normal to the shock and normal to the undisturbed inert/explosive interface has a unique value, being only a function of the HE/inert pair. This boundary angle serves as a boundary condition for the detonation, which, when combined with the $D_n(\kappa)$ law, provides a complete mathematical description for propagating

* Work supported by the United States Department of Energy

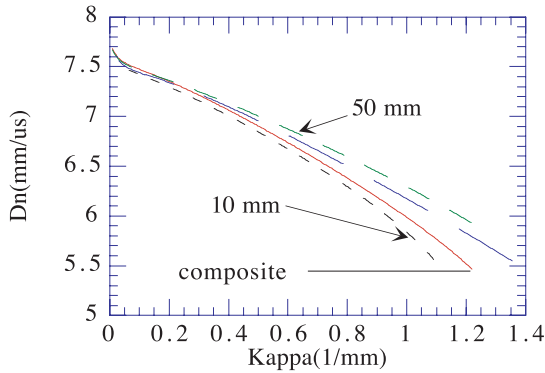


FIGURE 1. $D_n(\kappa)$ ALONG SHOCKS AT 3 RADII PLUS A COMPOSITE FIT, ALL FOR PBX 9502 AT 25°C. $D_{CJ} \approx 7.8\text{mm} / \mu\text{s}$

detonation in an explosive. An example of such a propagation law is the experimentally measured $D_n(\kappa)$ law for PBX 9502 described by us at the 11th Detonation Symposium^{1,2} and shown in Figure 1. The D_n vs κ overlay fairly well for different charge sizes.

Recent data on the nonideal explosive ANFO (density 0.88 gm/cc) shows the D_n vs κ along the shocks to be different from that shown in Figure 1. This data, shown in Figure 2, reveals little or no overlap of D_n vs κ for the various charge sizes. We discuss the data on ANFO in the section of this paper labeled **EXPERIMENTAL**. It is these structural differences from PBX 9502 and other ideal explosives that set ANFO apart as a nonideal. This data shows substantially larger departures of D_n from D_{CJ} , with the maximum measured detonation speed being far below D_{CJ} .

This difference in character for D_n vs κ along the shocks combined with our general interest in developing 1) a higher-order DSD theory and 2) a theory for explosives with highly state-sensitive, Arrhenius reaction rates, led us to develop extended theories. What distinguishes

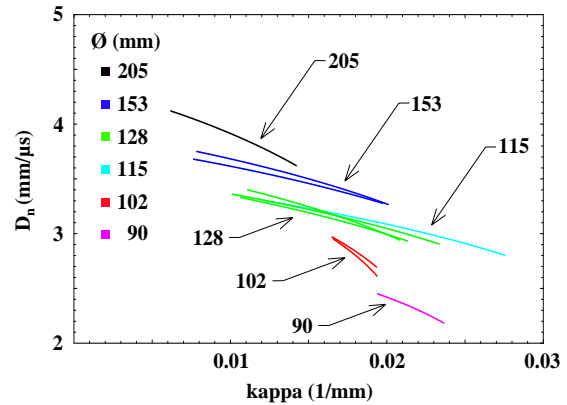


FIGURE 2. $D_n(\kappa)$ ALONG SHOCKS AT 6 RADII, ALL FOR AMBIENT TEMPERATURE ANFO LOT-20FEB2001. $D_{CJ} \approx 5.2\text{mm} / \mu\text{s}$

these extended theories from our earlier work is the inclusion of 1) higher-order terms in the perturbation expansion and 2) highly state-sensitive reaction rates. These in turn lead to more complex detonation front propagation laws. In addition to a dependence of D_n on κ , these laws contain contributions from shock acceleration, (DD_n/Dt) , and transverse flow, $(\partial^2 D_n / \partial \xi^2)$, where ξ is the arc length along the shock^{1,3}. We briefly describe these theories in the section of the paper labeled **THEORY**.

Using these theoretically derived propagation law forms as a guide, we develop a DSD calibration for ANFO based on the propagation law form

$$(1) \kappa_s + \frac{\sin(\phi)}{r} = F(D) - A(D) \frac{DD}{Dt} + B(D) \frac{\partial^2 D}{\partial \xi^2},$$

where $D = D_n / D_{CJ} - 1$, r = the radial coordinate and F , A and B are functions whose forms we select and then, in the section of the paper labeled **CALIBRATION**, fit to the rate stick data on ANFO. To demonstrate that such, more complex calibrated propagation laws are robust and useful for engineering

calculations, in the section labeled **3D LEVEL-SET CODE**, we use this propagation law to compute an explosive problem.

THEORY

Most rational theories of the multi-dimensional detonation reaction zone are based on the notion that the detonation departs from a planar, steady one-dimensional detonation by a small amount, hence, the notion of a perturbation theory for multi-dimensional detonation. We along with others have developed such theories^{1,3-6}, all based on the limit that the 1D, steady, Zeldovich-von Neumann-Doring (ZND) reaction-zone length, η_{rz} , is short compared to the radius of curvature of the detonation shock, $1/\kappa$. This serves to define a perturbation parameter, $\eta_{rz}\kappa = O(\varepsilon) \ll 1$. The idea then is that the detonation reaction zone is thin compared to all other problem scales and so, when viewed from the perspective of these other scales (charge size, etc.), it can be viewed as a front separating unburnt from burnt explosive. The dynamics of this subscale or front model is determined by solving for the interaction between the reaction zone and the system scale flow. This large-scale flow is controlled by the explosive geometry and by the conditions imposed on the high-explosive (HE) at its' boundaries. Although thin compared to the HE dimensions, the reaction zone is not vanishingly thin, but maintains a relative size, ε , which defines the distinguished limit we consider here. This theory develops a equation for how the normal velocity of propagation of the detonation front, D , depends on measures of the three-dimensionality of the flow, such as κ and $\partial^2 D / \partial \xi^2$, and on time dependence, as measured by the time rate of change in the shock normal direction,

DD / Dt . This is an intrinsic propagation law. Once solved for, it can be used to describe the progress of the front for all explosive geometry and boundary condition types. Besides the weak curvature assumption, this theory relies on the following properties of unsupported detonation for its' derivation. 1) The front moves into the unreacted HE at supersonic speeds, 2) in the reference frame of the detonation shock, the post reaction zone flow is supersonic, and thus the reaction zone is isolated from the post reaction zone flow, and 3) the detonation communicates with the environment only through where the edge of its' reaction zone meets the inert/HE boundary.

Based on an analysis of the reactive Euler equations

$$(2) \frac{\partial \rho}{\partial t} + \nabla \cdot (\rho \vec{u}) = 0,$$

$$(3) \frac{\partial \rho \vec{u}}{\partial t} + \nabla \cdot (\rho \vec{u} \vec{u} + \bar{I}P) = 0,$$

$$(4) \frac{\partial \rho e}{\partial t} + \nabla \cdot [(\rho e + P)\vec{u}] = 0,$$

$$(5) \frac{\partial \lambda_i}{\partial t} + \vec{u} \cdot \nabla \lambda_i = R_i(P, \rho, T, \lambda_1, \lambda_2, \dots, \lambda_N),$$

where $E(P, \rho, \lambda_1, \lambda_2, \dots, \lambda_N)$ is the specific internal energy, $e = E + \vec{u} \cdot \vec{u} / 2$, λ_i 's are the reaction progress variables, \vec{u} is the laboratory frame particle velocity, P is the pressure, ρ is the density and R_i are the reaction rates, we obtain the distinguished limit we seek by scaling the independent variables so as

$$(6) \tilde{t} = \varepsilon t, d\tilde{\xi} = \sqrt{\varepsilon} d\xi = \sqrt{\varepsilon} \left((dx)^2 + (dy)^2 \right)_+^{1/2}$$

where the + sign denotes variations along the shock, and where the important dependent variable scalings are

$$(7) \tilde{\phi} = \sqrt{\varepsilon} \phi, D = \varepsilon \tilde{D} = (D_n / D_{CJ} - 1),$$

with the tilded variables being the scaled variables. See Figure 3 for the variable definitions. The basic form we derive for the propagation law is a strong function of

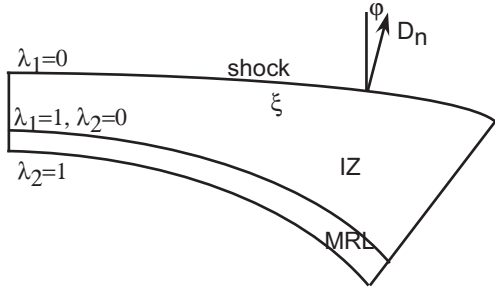


FIGURE 3. SCHEMA SHOWING REACTION ZONE FOR 2-STEP KINETICS MODEL. INTRINSIC COORDINATES AND VARIABLES ARE SHOWN.

the form of the rate law, R_i . We next describe the propagation laws derived for two different rate law forms.

P^n Rate Law

For the pressure dependent rate law form

$$(8) R_1 = k(P/P_{CJ})^n \sqrt{1 - \lambda_1},$$

where P_{CJ} is the Chapman-Jouguet pressure and k is the rate constant, we have carried the derivation of the theory through two orders in the perturbation parameter, ε . This was previously reported in the 11th Detonation Symposium¹. At $O(\varepsilon)$, the theory yields the classical $D_n(\kappa)$ front propagation law. At $O(\varepsilon^2)$, the theory yields corrections involving transverse flow and acceleration terms. Combining the $O(\varepsilon)$ and $O(\varepsilon^2)$ terms and removing the ε scalings, yields the higher-order propagation law

$$(9) \kappa_s + \frac{\sin(\phi)}{r} = F(D) - A(D) \frac{DD}{Dt} + B(D) \frac{\partial^2 D}{\partial \xi^2},$$

where $F(D)$, $A(D)$ and $B(D)$ are explicit functions derived in the theory.

To help with validation, we have performed high-resolution direct numerical simulations (DNS) of detonation in unconfined rate sticks and compared those results with theory for steady-state detonation. In the limit of steady detonation, we have

$$(10) D_n = D_0 \cos(\phi),$$

$$(11) \frac{DD}{Dt} = -D_{CJ} \left(\frac{D_0}{D_{CJ}} \sin(\phi) \right)^2 \kappa_s,$$

$$(12) \frac{\partial^2 D}{\partial \xi^2} = -\frac{D_0}{D_{CJ}} \left(\sin(\phi) \frac{d\kappa_s}{d\xi} + \cos(\phi) \kappa_s^2 \right),$$

so that we can rewrite Eq. (9) as a first-order ODE for κ_s . When combined with the equations defining the shock shape in terms of κ_s and ϕ , we have a system of three first-order ODEs for the steady-state detonation front, as it is described by Eq. (9)

$$(13) \kappa_s \frac{D_0}{D_{CJ}} \sin(\phi) \frac{d\kappa_s}{d\phi} = -\frac{D_0}{D_{CJ}} \cos(\phi) \kappa_s^2 - \frac{1}{B} \left\{ \kappa_s + \frac{\sin(\phi)}{r} - F - \left(\frac{D_0}{D_{CJ}} \sin(\phi) \right)^2 A \kappa_s \right\},$$

$$(14) \frac{dr}{d\phi} = \frac{\cos(\phi)}{\kappa_s},$$

$$(15) \frac{dz}{d\phi} = -\frac{\sin(\phi)}{\kappa_s},$$

where D_0 is the phase speed of the detonation and r and z are radial and shock displacement coordinates, respectively. Note, that Eq. (13) would be singular at $\phi = 0$ if the right hand side of Eq. (13) were nonzero at $\phi = 0$. This singularity is removed by setting κ_s such that the right hand side is zero at $\phi = 0$, which corresponds to an eigenvalue condition, $\kappa_{sc} \equiv \kappa_s(0)$, for this system of equations. Integrating this system of equations out to the prescribed edge boundary angle (corresponding to the inert confinement material selected) gives the

shock locus shape and detonation velocity as a function of rate stick radius.

For the validation, we used the polytropic fluid, mock solid HE model that we reported on previously¹. The parameters for the model are

$$(16) \rho_0 = 2 \text{ gm/cc}, \gamma = 3, D_{CJ} = 8 \text{ mm}/\mu\text{s},$$

$$n = 2, k = 1.2936 \mu\text{s}^{-1}, \eta_{rz} = 4 \text{ mm},$$

with a boundary angle, $\phi_e = 0.616$, corresponding to zero confinement. Displayed in Figure 4 is a comparison of the theoretical results and those obtained with high-resolution DNS using a Ghost-Fluid multi-material Euler solver⁷ in the *Amrita*⁸ DNS environment. The *Amrita* software provides us with patch based adaptive mesh refinement (AMR) and simulation scheduling (i.e., a utility for automating resolution and parameter studies). The dots with accompanying numbers indicate the DNS results and the number of mesh points in the stream-wise direction of the 1D, steady-state ZND reaction zone. Since the theoretical results were obtained with a perturbation theory referenced to the Chapman-Jouguet state, the comparison is quite favorable considering the size of the detonation velocity deficits being considered. Also noteworthy is the substantial differences in computed wave speed with resolution,

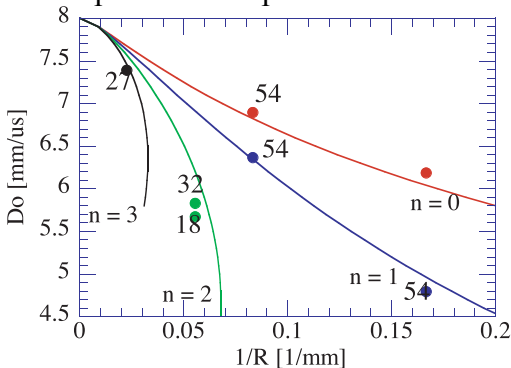


FIGURE 4. A COMPARISON OF THE DSD AND DNS DIAMETER EFFECT RESULTS FOR RATE PRESSURE EXPONENTS $N=0,1,2,3$.

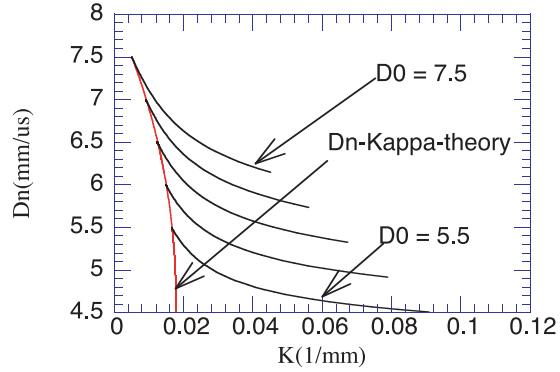


FIGURE 5. D_n vs κ_s ALONG INDIVIDUAL SHOCKS AND FOR THE BASE D_nK THEORY FOR THE REACTION RATE CASE OF $N=2$.

even with 32 points in the ZND reaction zone.

As we have noted previously, the differences between the base $D_n(\kappa)$ theory and higher-order theories is small when the admissible variation of the phase velocity for steady detonation is small. That this was the case for PBX 9502 is shown in Figure 1. The data for ANFO in Figure 2, shows that the D_n vs κ_s along different radii shocks do not overlay and that the admissible phase velocities vary significantly with stick radius. The question then is: how is D_n vs κ_s predicted to vary in the higher-order theory when large phase velocity differences are considered? Figure 5 shows the higher-order theory bares some similarity to the shock curvature data observed for ANFO. Based on these similarities, in the section labeled **CALIBRATION** we will use Eq. (9) to develop a DSD calibration for ANFO.

2-Step Arrhenius Rate Law

Our previous work has shown that for chemical reaction rates that have either low or moderate state sensitivity, the leading order DSD theory is a $D_n(\kappa)$ theory. Here we consider a chain-branching reaction model having two

components, where the first step is a thermally neutral induction step governed by a Arrhenius reaction with a large activation energy (the chain-branching step is called the IZ zone in Figure 3)

$$(17) R_1 = k_1 \exp\left(\frac{-1}{\varepsilon}\right) \exp\left(\frac{1}{\varepsilon} \left(1 - \frac{D_n}{D_{CJ}}\right)\right),$$

$$\text{with } \frac{1}{\varepsilon} = \frac{E_a}{D_{CJ}},$$

and the second step is a highly exothermic but state insensitive reaction (the chain-recombination step is called the MRL zone in Figure 3)

$$(18) R_2 = k_2 \sqrt{1 - \lambda_2},$$

and where ε is the order parameter defined earlier for the weak curvature limit. That is, we consider a distinguished limit in which $O(\varepsilon)$ variations of the curvature can lead to $O(1)$ variations in the induction zone rate and consequently in the induction-zone length. Since the curvature effects act in the induction zone, we expect that some of the shock acceleration and transverse flow effects that enter the theory at $O(\varepsilon^2)$ in the development in the previous sub-section, will be promoted to the $O(\varepsilon)$ theory. More details concerning this analysis can be found in Ref. 3.

With the same ansatz about the perturbation analysis that we made in the previous sub-section and that was used in Ref. 1, the $N = O(1)$ induction-zone length, is found to be

$$(19) N = -\tau \exp(-D),$$

where $0 \leq \tau \leq 1$ measures the induction-zone length relative to the overall reaction-zone length for the 1D, steady-state, ZND detonation. Since the IZ experiences $O(1)$ changes, this in turn leads to a large displacement of the MRL layer, and so has a large influence on where all the reaction energy is released. Proceeding with the $O(\varepsilon)$ MRL analysis,

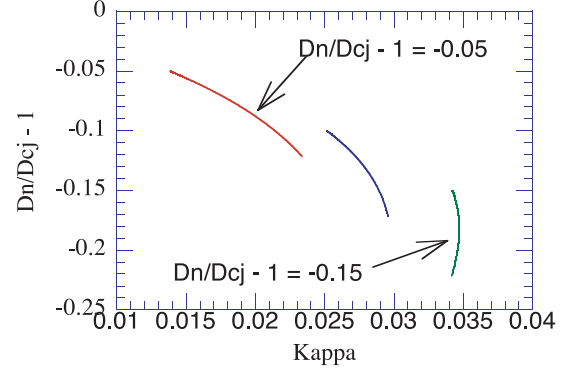


FIGURE 6. D_n vs κ_s ALONG INDIVIDUAL SHOCKS FOR THE 2-STEP REACTION RATE MODEL. DIMENSIONLESS VARIABLES ARE PLOTTED.

we find the leading-order DSD theory has become considerably richer

$$(20) -\alpha_1 D + \alpha_2 N \kappa_s - \alpha_3 \kappa_s + \alpha_4 \frac{DN}{Dt} - \alpha_5 \left(\frac{\partial N}{\partial \xi}\right)^2 - \alpha_6 \frac{\partial^2 N}{\partial \xi^2} = 0,$$

where the α_i 's are non-negative constants whose values are derived in the theory. Thus, high reaction state sensitivity has promoted acceleration and transverse flow effects into the leading-order theory.

As in the previous sub-section, we can use this propagation law to compute the rate stick problem. Shown in Figure 6 are the results of such a calculation for the strong-shock limit of the model explosive (21) $\gamma = 3, \tau = 0.5, \phi_e = 0.38$.

The D_n vs κ_s for this rate-law model is very different from the results shown in Figure 5. The curvature is nearly constant along some of the shocks while D_n undergoes considerable variation. Some of the ANFO data which has been reported on previously¹¹, show some of these trends. These results come with one important caveat, preliminary indications are that Eq. (20) leads to unstable detonation propagation when time dependence is allowed.

In the next section, we describe the rate stick experiments that have been done to characterize ANFO.

EXPERIMENTS

Our ANFO was composed of commercial (Titan Energy, Lot No. 20FEB2001) explosive grade AN prills, with 6 wt.% diesel fuel. Separate bags were well blended prior to firing, to obtain consistent samples and to minimize batch-to-batch variability.

Twelve rate sticks were fired at ambient temperature in thin wall (6 mm) paper tubes. Seven diameters were tested between 77 and 205 mm inner diameter (ID). Three cases were successfully repeated to obtain duplicate front curvatures. The length-to-diameter (L/D) ratio was 10 in all cases. The charges were fired in a vertical position to 1) accommodate top loading, 2) record detonation front curvature at the bottom, and 3) obtain an axially symmetric density distribution to minimize wave tilt. A schematic diagram is shown in Figure 7.

Each charge was loaded in ten separate lifts—except for the 205 mm stick, which required twenty lifts—to attain a uniform density throughout the charge. Individual lifts were weighed prior to pouring. During the pour of each lift, the outside of the tube was gently tapped. The top of each lift was lightly tamped with a flat-bottomed plunger to provide a level prill distribution between lifts. The rise height of each lift was measured and the density per lift calculated. This procedure gave a bulk density of approximately 0.88 gm/cc. The shots were boosted using pressed PBX 9501 cylinders. These had the same ID as the tubes, and a L/D ratio of 1/2.

The detonation velocity was measured using eleven self-shortening capped shock pins glued into holes drilled at equal intervals along the tube. The

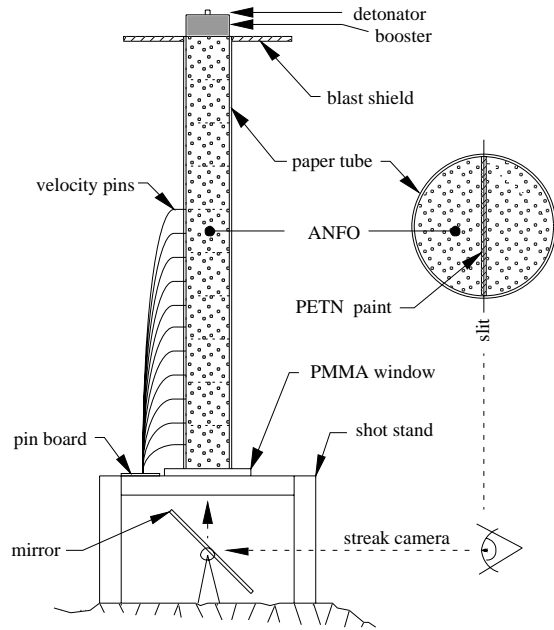


FIGURE 7. SCHEMA OF ANFO RATE STICK EXPERIMENT.

shorting pins were inserted flush with the ID of the tube starting four diameters from the top of the rate stick. The eleven shorting pins were connected to a Los Alamos DM-11 pin board and multiplexed to a single cable so that when the detonation wave shorts the pin, it fires an RC circuit in the pin board, producing a short voltage pulse.

To measure detonation front curvature, the rate sticks were capped at the bottom with a PMMA window. A small strip of PETN paint was applied across the diameter of the inside window surface; this served as a flasher. It was applied in a thin layer and covered with copper tape to block reaction pre-light from the detonation front, which scatters 20 to 30 mm ahead of the wave front.¹⁰ The front curvature was recorded with a rotating mirror streak camera at a writing speed of 1 mm/ μ sec. Displayed in Figure 8 is an example of a measured streak-camera trace of the shock front shape.

The film records were read on an optical comparator from edge to edge.

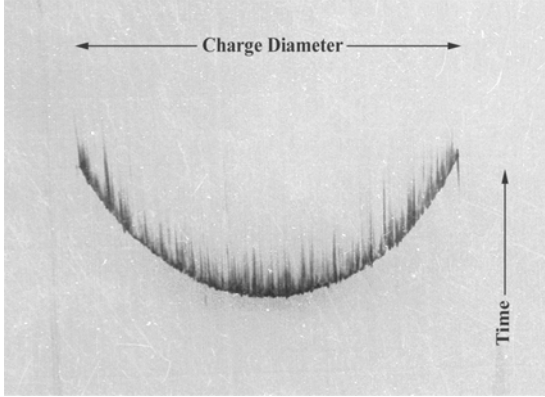


FIGURE 8. STREAK-CAMERA TRACE OF AN ANFO SHOCK.

The charge center was defined as the midpoint between the two edges. The magnification was inferred from the measured tube ID recorded in the pre-shot still. Shock traces were recorded for 205, 153, 128, 115, 102 and 90 mm diameter charges. This data was reduced to give D_n vs κ_s along each measured shock, in the manner described in Ref. 2. Those results are displayed in Fig. 2. The measured value of shock-edge angle was $\phi_e \approx 29^\circ$. A linear least-squares fit was applied to the $x-t$ pin data to obtain the phase velocity, D_0 , for each rate stick.

Measurements were also made on a second ANFO lot (Titan Energy, Lot No. 30SE99C), with a density 0.90 gm/cc, that was nominally the same formulation as Lot No. 20FEB2001. Lot No. 30SE99C was stored in a magazine for over a year and experienced some separation of fuel oil from the AN prills, having 5 wt.% of diesel fuel when fired. The measured detonation velocities were similar for both lots. They are collected and displayed in Figure 9. The D_n vs κ_s along the shocks for Lot No. 30SE99C were very different from the results presented in Figure 2 and are described in detail in Ref. 11.

In the next section we describe how the data for ANFO lot-20FEB2001 was calibrated to the propagation law

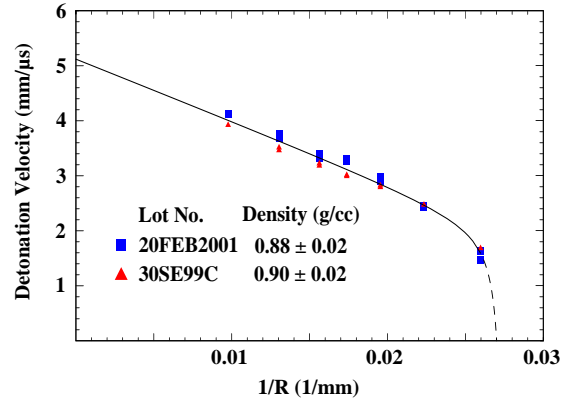


FIGURE 9. DETONATION PHASE VELOCITY DATA FOR 2 ANFO LOTS.

form given by Eq. (9).

CALIBRATION

In all DSD calibration work, the assumption is made that a single set of functions ($A(D)$, $B(D)$ and $F(D)$) and parameters (D_{CJ} and ϕ_e) can be found that fit all of the available data for an explosive formulation. To maintain stability and regularity in the Eq. (9) modeling form, this fitting must be constrained such that $A(D) \geq 0$, $B(D) \geq 0$, $F(D) > 0$, $D_{CJ} > 0$ and $\phi_e > 0$. Otherwise, we have considerable flexibility in selecting the functions used. Some advantage is gained by selecting forms that have some basis in theory, since they bring with them the underlying structure in the problem. This is the approach we follow here in selecting the following forms for calibration

$$(22) F(D) = -E1 \cdot D \cdot (D + 1 - B1)^{A1} \cdot \exp(-C1/(D + 1 + D1)),$$

$$(23) A(D) = E2 \cdot \left(\frac{1 - A2 \cdot D + C2 \cdot D^2}{1 - B2 \cdot D + D2 \cdot D^2} \right),$$

$$(23) B(D) = E3 \cdot \left(\frac{1 - A3 \cdot D + C3 \cdot D^2}{1 - B3 \cdot D + D3 \cdot D^2} \right),$$

where the constants $A1 \geq 0, \dots D3 \geq 0$ and where Eq. (22) supports the idea of a critical curvature, i.e., F has a maximum in the range $0 < D < 1$.

With these functions specified, Eqs. (13-15) can be integrated to get the diameter effect and shock shapes, once appropriate initial and boundary conditions are supplied. We integrate the equations from $\phi=0$, where we supply the initial data

$$(24) \kappa_s(0) = \kappa_{sc} + G \cdot \phi^2 + \dots$$

$$(25) r(0) = 0 \text{ and } z(0) = 0,$$

to $\phi = \phi_e$, where no condition need be applied. The constants κ_{sc} and G are determined via a local analysis of Eqs. (13-15) carried out in the vicinity of $\phi=0$. The local solution, given by Eq. (24), is used for $0 \leq \phi \leq \delta$ (with δ small), after which the solution is carried out using a standard numerical ODE solver.

These numerically generated solutions are then systematically fit to the composite experimental data set, which consists of the phase velocities and the shock shapes (i.e., z vs r for the shocks shown in Figure 2), using a Levenberg-Marquardt, nonlinear least squares algorithm. To get a meaningful numerical Jacobian, a matrix which describes how the components of the computed solution vary with the changes in the parameters, the computed solution has to be highly accurate, with relative errors less than 10^{-10} .

Since the diameter effect and shock shape data sets contain very different numbers of data points, weighting functions need to be selected to determine the contributions each should make to the merit function, M , that is to be minimized for the fit

$$(26) M = \sum_i E_i^2, \quad i = 1, \dots, m.$$

Here m is the number of independent data points and the E_i 's for the diameter effect and shock shape data points are respectively

$$(27) E_i = W_R \cdot \frac{[R_i(calc) - R_i(exp)]}{R_i(exp)},$$

$$(28) E_i = W_S \cdot \frac{[Z_{ij}(calc) - Z_{ij}(exp)]}{R_j(exp)}.$$

The constants W_R and W_S are the weighting factors for the diameter and shock data and $R_i(exp)$ is the experimental charge radius, $R_i(calc)$ is the calculated radius, $Z_{ij}(exp)$ is the shock displacement for the i -th point on the j -th charge and $Z_{ij}(calc)$ is the calculated displacement.

An examination of the right hand side of Eq. (13) reveals that to have the term containing A be the same order as $(\kappa_s + \sin(\phi)/r)$, then $A \approx 10$. Given that the factor $((D_0/D_{CJ}) \cdot \sin(\phi))^2$ keeps the A term small over most of the charge radius, this term generally will not impact the calculation of the diameter effect by much. Although the B containing term has a more global reach, it must be of the order $B \approx (D_{CJ}/D_0)/\kappa_s \approx 100$ to play a significant role in the fits to the ANFO data.

In performing our parameter optimization, we have set $A2 = 0, B2 = 0, C2 = 0, D2 = 0, A3 = 0, B3 = 0, C3 = 0, D3 = 0, W_R = 50, W_S = 100, \phi_e = 0.5$ and $D_{CJ} = 5.2 \text{ mm}/\mu\text{s}$, where the D_{CJ} value is suggested by the fit in Figure 9. With these choices, the optimization returns

$$(29) E1 = 0.04229 \text{ mm}^{-1}, \quad A1 = 0.0,$$

$$C1 = 0.06886, \quad B1 = 0.5824, \quad D1 = 0.00012,$$

$$(30) E2 = 9.5231, \quad E3 = 28.4179 \text{ mm}.$$

Displayed in Figure 10 is a comparison of the shock shapes computed from the calibration and the shock shape data. The calibration is very good, as can be

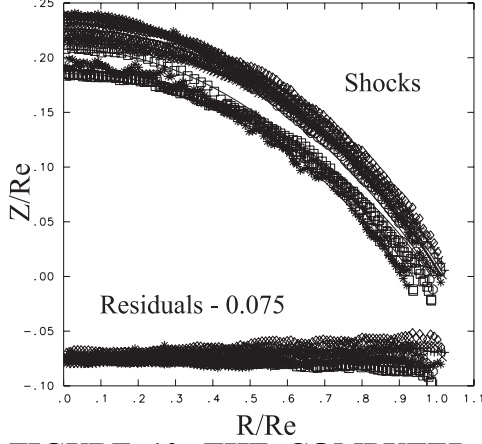


FIGURE 10. THE COMPUTED AND EXPERIMENTAL SHOCKS AND FIT RESIDUALS.

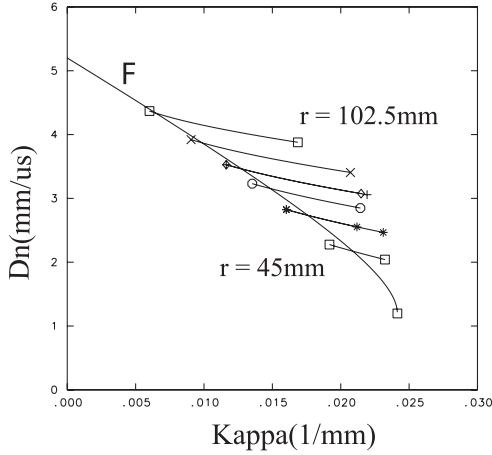


FIGURE 11. D_n vs κ_s ALONG THE SHOCKS AND THE $\kappa = F(D)$ CURVE.

seen by the residual level (the residuals are offset by -0.075 to facilitate plotting). A summary of the results from the model for D_n vs κ_s along each individual shock and the for the underlying $D_n(\kappa)$ terms in the model, is shown in Figure 11. As should be clear, both the acceleration, $A(D)$, and transverse, $B(D)$, terms play significant roles in the DSD calibration for ANFO.

In the next section, we give an example of detonation front evolution using this ANFO calibration. Our new 3D

front tracking code, based on level-set methods, is utilized for this purpose.

3D LEVEL-SET CODE

Our group has used DSD front propagation codes, based on level-set methods, for some time.¹² Recently, we have extended these methods to treat higher-order propagation models. We have also developed new, robust numerical algorithms for applying DSD boundary conditions, which are suitable for handling complex, 3D HE geometries. Drawing on these developments, we have built a general purpose, 3D DSD front propagation code based on an extension of the level-set method. Two important new features included in this code are: 1) a method for establishing a priority order for setting the values of ghost nodes, that permits each ghost node to be set via an explicit evaluation (i.e., no iteration) and 2) a modification of the level-set formulation that allows us to imbed Eq. (9) in a second level-set field. Ghost nodes (computational nodes immediately adjacent to the HE region) are used to set boundary conditions.

The extended level-set method solves the following two equations

$$(31) \frac{\partial G}{\partial t} + D_n(\vec{n} \cdot \nabla(G)) =$$

$$\frac{S(\psi)}{\varepsilon_2} \cdot (\sigma_2 - \vec{n} \cdot \nabla(G)) - \frac{D_{CL}}{A(G)} \cdot \left(\kappa - F - B(G) \cdot \frac{\partial^2 G}{\partial \xi^2} \right)$$

and

$$(32) \frac{\partial \psi}{\partial t} + D_n |\nabla(\psi)| = \frac{S(\psi)}{\varepsilon_1} \cdot (\sigma_1 - |\nabla(\psi)|),$$

where $S(\psi)$ is a Heaviside function

$$(33) S(\psi) = \frac{\psi}{\sqrt{\varepsilon_3 + \psi^2}},$$

and where ψ is the level-set function that imbeds the detonation front location (with

the level $\psi=0$ representing the detonation front location), G is the level-set function that imbeds the detonation front speed ($G(\psi=0)=0$ gives the speed at the front location) and $\varepsilon_1, \dots, \varepsilon_3$ are small parameters. The first terms on the right hand side of Eqs (31-32) act to maintain the gradient of the level-set functions at specified constants; at σ_1 for Eq. (32) and at σ_2 for Eq. (31). The advantages of using a level-set formulation are discussed in Ref. 12.



FIGURE 12. 3D DSD CALCULATION OF ANFO RATE STICK USING EQ. (9).

Using this extended, 3D level-set code, we show that Eq. (9) and the Eqs. (29-30) ANFO calibration produces a stable propagating detonation. We consider the problem of detonation in a 200 mm diameter rate stick and subject to an edge angle of $\phi_e = 0.5$. The detonation front, captured at a number of different times as the detonation proceeds up the stick, is displayed in Figure 12.

REFERENCES

[1] T. D. Aslam, J. B. Bdzil and L. G. Hill. Extensions to DSD theory: analysis of pbx 9502 rate stick data. In *Eleventh Symposium (Int.) on Detonation*, pages

21-29, Snowmass, CO, 1998. Office of Naval Research, ONR 33300-5.

[2] L. G. Hill, J. B. Bdzil and T. D. Aslam. Front curvature rate stick measurements and detonation shock dynamics calibration for pbx 9502 over a wide temperature range. In *Eleventh Symposium (Int.) on Detonation*, pages 1029-37, Snowmass, CO, 1998. Office of Naval Research, ONR 33300-5.

[3] M. Short and J. B. Bdzil, Propagation laws for steady curved detonations with chain-branching kinetics. *J. Fluid Mech.*, accepted for publication 2002.

[4] J. B. Bdzil. *J. Fluid Mech.*, 108:195, 1981.

[5] R. Klein. On the dynamics of weakly curved detonations, IMA volumes in Mathematics and its Applications, 35: 127-66, 1991.

[6] J. B. Bdzil, W. Fickett and D. S. Stewart. Detonation shock dynamics: A new approach to modeling multi-dimensional detonation waves. In *Ninth Symposium (Int.) on Detonation*, pages 730-42, Portland, OR, 1989. Office of Naval Research, OCNR 113291-7.

[7] R. P. Fedkiw, T. D. Aslam, B. Merriman and S. Osher. *J. Comput. Phys.*, 152:457-92, 1999.

[8] J. J. Quirk. A parallel adaptive grid algorithm for computational shock hydrodynamics, *Applied Numerical Mathematics*, 20-4:427-53, 1996.

[9] R. Klein and D. S. Stewart. *SIAM J. Appl. Math.*, 53-5:1401-35, 1993.

[10] D. L. Kennedy. Private communication, 2000.

[11] R. A. Catanach and L. G. Hill. Diameter effect curve and detonation front curvature measurements for anfo. In *Shock Compression of Condensed Matter – 2001*, pages xxx-xx, Atlanta, GA, 2001, AIP Conference Proceedings.

[12] T. D. Aslam, J. B. Bdzil and D. S. Stewart. *J. Comput. Phys.*, 126:390, 1996.